ARL-TR-9211 • MAY 2021

DEVCOM ARMY RESEARCH LABORATORY

# Monochromatic Laser-Induced Shockwave Measurements with Improved Data Processing for Reactive Materials

by Elliot R Wainwright and Jennifer L Gottfried

## NOTICES

### Disclaimers

The findings in this report are not to be construed as an official Department of the Army position unless so designated by other authorized documents.

Citation of manufacturer's or trade names does not constitute an official endorsement or approval of the use thereof.

Destroy this report when it is no longer needed. Do not return it to the originator.

ARL-TR-9211 ● MAY 2021

# Monochromatic Laser-Induced Shockwave Measurements with Improved Data Processing for Reactive Materials

**Elliot R Wainwright and Jennifer L Gottfried**
*Weapons and Materials Research Directorate,*
*DEVCOM Army Research Laboratory*

# REPORT DOCUMENTATION PAGE

*Form Approved*
*OMB No. 0704-0188*



| 1. REPORT DATE *(DD-MM-YYYY)* | 2. REPORT TYPE | 3. DATES COVERED (From - To) |
|---|---|---|
| May 2021 | Technical Report | October 2020–May 2021 |

**4. TITLE AND SUBTITLE**
Monochromatic Laser-Induced Shockwave Measurements with Improved Data Processing for Reactive Materials

**5a. CONTRACT NUMBER**

**5b. GRANT NUMBER**

**5c. PROGRAM ELEMENT NUMBER**

**6. AUTHOR(S)**
Elliot R Wainwright and Jennifer L Gottfried

**5d. PROJECT NUMBER**

**5e. TASK NUMBER**

**5f. WORK UNIT NUMBER**

**7. PERFORMING ORGANIZATION NAME(S) AND ADDRESS(ES)**
DEVCOM Army Research Laboratory
ATTN: FCDD-RLW-WA
Aberdeen Proving Ground, MD 21005

**8. PERFORMING ORGANIZATION REPORT NUMBER**
ARL-TR-9211

**9. SPONSORING/MONITORING AGENCY NAME(S) AND ADDRESS(ES)**

**10. SPONSOR/MONITOR'S ACRONYM(S)**

**11. SPONSOR/MONITOR'S REPORT NUMBER(S)**

**12. DISTRIBUTION/AVAILABILITY STATEMENT**
Approved for public release; distribution unlimited.

**13. SUPPLEMENTARY NOTES**
ORCID IDs: Elliot R Wainwright, 0000-0002-2301-9420; Jennifer L Gottfried, 0000-0002-1282-1928

**14. ABSTRACT**

We present enhanced measurement and data-processing techniques for a modified laser-induced air shock from energetic materials (LASEM) system. This system was recently upgraded with a 640-nm imaging laser and monochromatic high-speed camera, which, when combined, allows for higher frame-rate imaging and the ability to penetrate through the optically thick plasma at early times (<10 μs). We implement an automated shockwave detection code via MATLAB that improves the throughput of data analysis speed by over 10×. We present the efficacy of various models and empirical fits using the higher frame-rate data. The characteristic shock velocity is analyzed across various time intercepts and beam energies and optimal settings are discussed. Only small changes in the characteristic velocity are observed over a roughly approximately 150-mJ laser energy range near the standard operating value. A suite of powdered metal samples has been analyzed using the upgraded system, which demonstrates the ability for the system to differentiate performance across an array of materials. Results from the new system correlate well to previous iterations. The upgrades allow for the rapid assessment tool for the microsecond energy release of reactive materials, particularly for samples with subtle performance differences (e.g., metal particles with varying sizes).

**15. SUBJECT TERMS**
laser-induced air shock from energetic materials; LASEM; shockwave detection; laser-induced plasma; schlieren imaging; reactive materials

| 16. SECURITY CLASSIFICATION OF: | | | 17. LIMITATION OF ABSTRACT | 18. NUMBER OF PAGES | 19a. NAME OF RESPONSIBLE PERSON |
|---|---|---|---|---|---|
| a. REPORT | b. ABSTRACT | c. THIS PAGE | | | 19b. TELEPHONE NUMBER (Include area code) |
| Unclassified | Unclassified | Unclassified | UU | 33 | Elliot R Wainwright<br>443-371-6717 |

## Contents

## List of Figures

## List of Tables

## Acknowledgments

This work was supported in part by the US Department of Defense, Office of the Under Secretary for Defense for Research and Engineering, Applied Research for the Advancement of S&T Priorities Program on Enhanced Energetic Effects and by the US Army Combat Capabilities Development Command Army Research Laboratory's 6.2 project "Explosives for Long Range Cooperative Engagements" under the Long Range Distributive and Cooperative Engagements Essential Research Program. The authors thank Frank De Lucia for his feedback and helpful experimental insight, Brian Barnes for his suggestions on data analysis, and Steven Dean for the initial construction of the experimental apparatus.

## 1. Introduction

Laser-induced air shockwaves can be used as a relative metric for microsecond-scale energy release of reactive and energetic materials. The laser-induced air shock from energetic materials (LASEM) method, which uses a high-energy laser pulse to ablate and excite small quantities (mg) of material, has shown good correlations with energetic material performance metrics at much larger scales under detonation conditions, particularly for high-explosive (HE) materials.[1–5] Recent efforts have been made to use LASEM on metal-based reactive materials,[6–10] where efforts to upgrade the diagnostics on the system (e.g., temporal resolution) are paramount.[11] Such improvements in diagnostics are necessary to sparse out otherwise small differences in performance by materials of similar chemistry, size, or microstructure. In addition, some of the materials of interest display bright emission in the visual spectrum at early times (e.g., from metal emission features), and specialized imaging techniques are needed to visualize the shockwave through the optically dense plasma. As diagnostics improve, for example with higher camera frame rates, previously established data-processing techniques become more time consuming and burdensome and methodologies to improve the data-processing speed and throughput are needed. One way to achieve this higher throughput is to use automated edge-detection algorithms to track the air shockwave propagation without human intervention. The corresponding LASEM experimental system must be properly timed and triggered to generate repeatable data via consistent laser pulse timing, coupled with imaging techniques that penetrate through the optically thick plasma at earlier times.

Here, we present experimental upgrades made on the US Army Combat Capabilities Development Command Army Research Laboratory's LASEM system. To differentiate measurements made here from previous LASEM results, we colloquially call the new setup monochromatic LASEM, or m-LASEM, as they operate on the same principles. With this upgraded m-LASEM system, we use a spoiled-coherence imaging laser and monochrome high-speed camera to measure the air shockwave earlier in the plasma lifetime at 800,000 frames per second (fps), double the previous LASEM limit used in this lab. While a variety of other optical diagnostics are used on LASEM and m-LASEM, including spectroscopy and other optical measurements, here we discuss primarily the imaging and shockwave detection. Data from the initial LASEM system has been reported previously,[12] but the experimental design has since been upgraded significantly. The complexities of the triggering and response times of each component of m-LASEM are presented for ease of reference. We detail the new imaging and diagnostic capabilities, the triggering and timing setup of the system, and present a simple MATLAB code that

is used to automatically detect and track the laser-induced shockwave. Further, we discuss the automated fitting of said data to various theoretical models and empirical fittings and discuss the benefits of each. We also discuss how these methods differ from the well-established LASEM system published previously.[1,11] Finally, we present a correlation of laser-induced air shockwave velocity data between the existing LASEM system and m-LASEM that speaks to the fidelity of the measurements made on the new system.

## 2. Experimental System and Results

### 2.1 m-LASEM: Triggering and Timing

LASEM uses a Z-type schlieren imaging system to capture the laser-induced air shockwave. The laser-induced plasma is initiated by a high-power Q-switch laser (Brilliant B, 1064 nm, 900 mJ max, 6-ns pulse), which has a typical laser output energy near 660 mJ after the optics train. Here, for m-LASEM, a Photron SA-Z monochrome high-speed camera is used at 800,000 fps at the minimum exposure time of 159 ns. At such high speeds the frame resolution is limited to 524 × 24 pixels. The quality of the schlieren images can be affected by a variety of properties, including light percent cut off by the knife edge, the half-angle of the Z system, the distance from the pinhole to the first parabolic mirror, and other factors.[13] A spoiled-coherence imaging SI-LUX640 laser (Specialized Imaging, 640 ±6 nm) is used as the light source for the schlieren imaging. A bandpass filter (custom filter with SI-LUX, peak at 647.3 ±5 nm) is used in front of the camera's imaging lens to remove any effects of ambient light and emission from the plasma. A schematic of the imaging apparatus is shown in Fig. 1. This imaging laser can operate up to 10 MHz and a maximum of 400 W, and experiences a tradeoff in number of pulses and the width of each being limited to an overall maximum "on" time of 30 μs. Thus, the higher the pulse rate (i.e., shorter pulse width), the lower the laser energy per pulse and the shorter the "on" time for the laser.

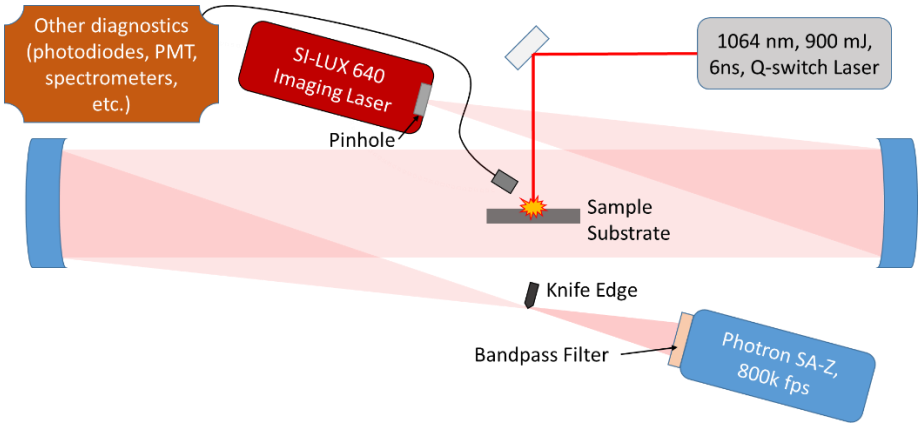


**Fig. 1 Schematic of the Z-type schlieren imaging apparatus used with m-LASEM**

The triggering and timing of the system is controlled in its entirety by two digital delay generators (DDGs) (Berkeley Nucleonics Model 575), which we denote as DDGA and DDGB. The triggering array is shown schematically in Fig. 2. Most importantly, the first delay generator (DDGA) has its internal clock synced to that of the laser flashlamp at 10 Hz. It also triggers the Q-switch laser pulse that leads the firing of the laser. DDGA also triggers all of the miscellaneous diagnostics that may be included in the system (including spectrometers, photodiodes and photomultiplier tubes [PMTs], other imaging cameras, etc.), which are all timed relative to the Q-switch triggering pulse. Thus, the master signal of the whole triggering array is the Q-switch pulse. We include a 0.1-s delay on the Q-switch pulse such that the entire system fires simultaneously with the next flashlamp 10-Hz pulse. The Q-switch pulse triggers the SA-Z, which is set in the camera software to use a Random Reset trigger input. This method automatically resets the internal clock/frame buffering of the camera to align with the trigger pulse. The camera then outputs a positive voltage pulse that serves as the trigger input for the second delay generator: DDGB. DDGB has its internal clock frequency set at the camera frame rate. DDGB is then used primarily as a pulse generator, set to burst mode with 150 pulses to serve as the triggering pulse train for the SI-LUX laser. The associated “laser-on” imaging pulse width for these conditions is 200 ns per pulse.

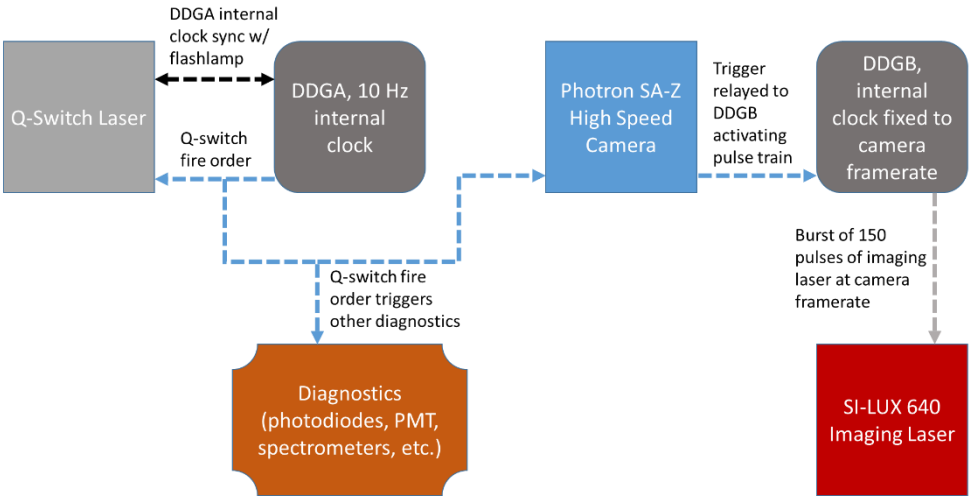


**Fig. 2 Triggering diagram for the m-LASEM**

Each component of this system has its own inherent electronic and power response times, including delays in rise-to-maxima (for example, with the laser pulse) or software delays. With the goal of aligning the actual laser firing event with the start of the camera frame and imaging laser pulse, these delay times must be meticulously tracked and accounted for. The timing diagram of the system is shown in Fig. 3, which denotes the assigned delay times in the delay generators and the associated camera numbers and frame descriptions. There is a 1.7-µs delay from the triggering of the camera in Random Reset mode to the start of the first exposure. Further, there is a 0.6-µs pulse delay to the start of the laser firing, and a farther 45 ns to the peak power of the laser. The full width half maximum of the laser pulse is 6 ns. Thus, the camera delay time is set such that the start of the first frame is aligned with just after the firing of the laser, which corresponds to approximately 2.4 µs (i.e., 0.6 + 1.7 µs). The imaging laser also has an approximately 10-ns rise time, approximately 5-ns jitter, and approximately 70-ns input-to-light pulse delay, which is roughly 10× less than the firing delay for the Q-switch laser. There is no added delay to the SI-LUX triggering. The input trigger from DDGA is relayed through the camera (with an associated delay time of 90 ns) to the General Output port. By accounting for these various delay and response times, we ensure a consistent sequence of events per frame each shot, including the initial plasma and shockwave, meaning that differences in the shock position are only due to material contributions and not temporal uncertainty.

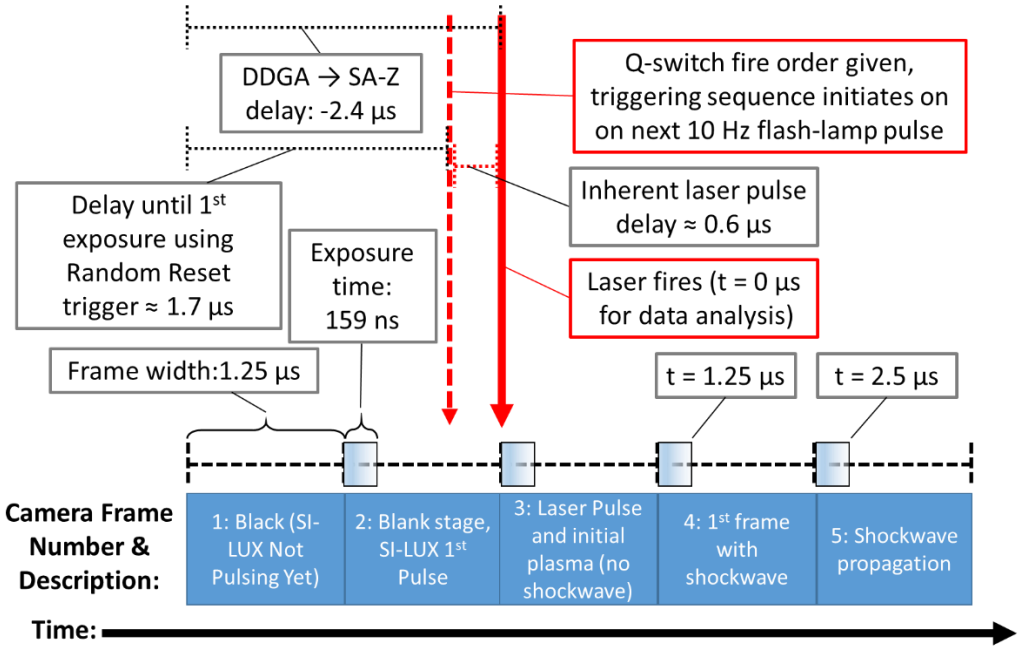


**Fig. 3 Timing diagram for the upgraded LASEM system, including inherent electronic and triggering delays overlaid with the observation in the camera frame at each time step**

Representative stills from the schlieren videos are shown in Fig. 4, which compares the laser-induced plasma and shockwave from the blank tape (Fig. 4a) and a micron-sized aluminum (Al) powder (Fig. 4b). This timing generally results in consistent size and shape of the plasma in the first frame, with differences in the shockwave measurable thereafter. Variations in the background are due to SI-LUX intensity variability and timing between pulses. Occasionally debris, ejected particulates, or density/thermal gradients can be observed as dark bands within the plasma. At later times (generally >50 µs) powder-based samples exhibit streaking as particles ejected by the shockwave move through (and ignite, if the sample is sensitive enough) in the hot gas above the substrate. Such streaking can be observed in the last time-step frame of Fig. 4b. It is clear from Fig. 4 that imaging with the spoiled coherence laser aids considerably in piercing through the optically thick plasma to observe the shockwave at earlier times (i.e., <10 µs). From these frames we can extract position (and therefore velocity) of the shockwave in air and qualitatively compare the other gradients in index of refraction (i.e., temperature, size, and shape of the hot plasma gases). Given a fixed exposure time, the width of the shockwave could also be used to make velocity measurements, but this method is currently limited by the relatively low pixel numbers/spatial resolution used at this camera frame rate of 800,000 fps.

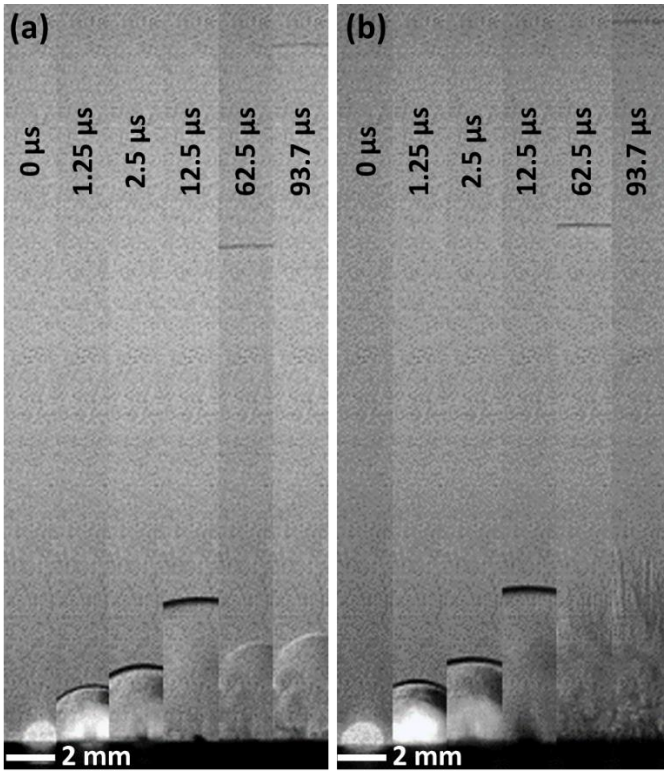


**Fig. 4 Schlieren image stills of a) blank tape and b) µm-scale Al powder, demonstrating shockwave formation and propagation**

## 2.2 MATLAB Processing of Shockwave Images

Typically, the air-shock velocity measurements for a given sample are averaged over 20 individual laser shots of the material, with each shot composed of at least 120 frames. Thus, with over 2400 frames per sample to analyze, fast, automated methods must be utilized. The major novelty of this work is the automated image processing and edge detection that is feasible under these imaging conditions. Using the analysis scheme as prescribed in the following, we are able to measure, fit, analyze, average, and calculate the confidence interval of all 2400 frames in roughly 10–20 min. Such analysis by hand could take days or even weeks.

The framework for the shock fitting uses and is inherent to the MATLAB image-processing toolbox. The basic operation of the code batch processes through entire folders of data without user intervention and compiles the results into a single Microsoft Excel document. The code operates by measuring the distance between the top of the sample slide and the shock velocity using edge-detection algorithms. While there are several algorithms to choose from in MATLAB, we determined that the “Canny” detection scheme with a threshold of 0.3 and sigma value of 1 accurately and consistently measures the position of both the front and back edge of the shockwave with a width of 1 pixel. In principle, these algorithms work by

measuring gradients in intensity in the x-axis or y-axis directions, or at some fixed angle relative to the frame. The Canny algorithm operates by using a high and low threshold and the derivative of a Gaussian filter to detect edges.[14] Once the edges have been detected, the image is cleaned of any edges that are less than 20 pixels in total size, which generally removes any noise. The shockwave position is then measured as the farthest edge detected away from the sample slide/stage. An example of the edge-detection scheme applied to shockwave images and the corresponding position/shockwave radius trace are shown in Fig. 5. The detected edges are shown in pink in Fig. 5a, where the edges behind the shock front are ignored. There is no preprocessing of the video frames such as contrast enhancement or de-speckling necessary prior to analysis.

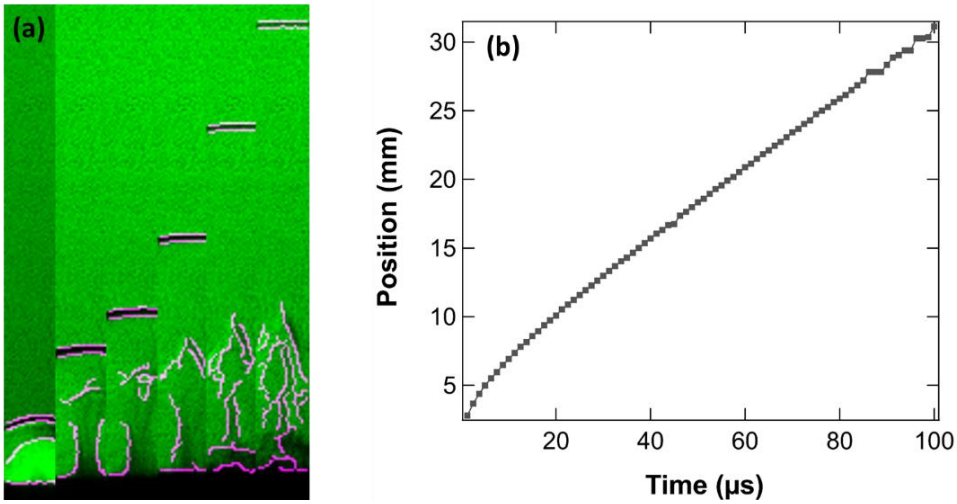


**Fig. 5 a) Edges detected by the custom MATLAB code (pink) overlaid with the original schlieren image (green); b) representative position vs. time trace demonstrating slowing of the shockwave to a steady velocity. Data from a representative μm-sized Al powder sample.**

Once the position versus time trace has been established, nearly all data analysis can follow directly from it. Unlike previous iterations of LASEM, which have used a backwards-difference instantaneous velocity measurement,[15] m-LASEM uses a velocity measurement drawn relative to the stage position and total time elapsed. Such a method reduces the overall uncertainty in position as time progresses and generates smooth position/radius curves as shown in Fig. 5b. The oscillations and jumps in the position from 90–100 μs are a result of the shockwave fading into the background (i.e., low signal-to-noise in the camera frame) and thus the shockwave measurement jumping between the back and front edge of the shockwave instead of being drawn consistently from the front. Such oscillations have very little effect on any data fitting. Typically, a threshold of minimum number of data points is set for a laser shot to be considered adequate for analysis. This threshold is usually set to 70%–80% of the total camera frames for a given shot having a detectable

shockwave. By establishing such a threshold, the effect of data trace length in time from shot-to-shot variation is mitigated. It also requires additional shots be taken for materials with weaker shockwaves, such as blank tape and inert powders, to establish similar confidence intervals for those samples.

We know microsecond-scale reactions with entrained oxygen can occur while the shockwave is still being influenced with the plasma.[16] Tracking only the first-position pixel for a variety of samples provides an understanding of the resolution limits and sensitivity of the system and emphasizes the importance of material reactions occurring later in time in the laser-induced plasma. Under the current conditions, a difference in position/radius of 1 pixel corresponds to roughly 35 m/s, and we observe differences in the first frame velocity between nm-sized and micron-sized Al powder of roughly 1–3 pixels. This increase is in addition to a roughly 6-pixel increase over the blank substrate and tape without reactive material. We know that μm-Al has a significantly lower laser-induced shock velocity than nm-Al. Thus, if one were to only look at the earliest time data point (i.e., 1.25 μs), before accounting for the chemical reactions within the rapidly cooling laser-induced plasma over multiple microseconds, these samples would look effectively the same. Therefore, a full time-series data fitting and careful choice of the characteristic velocity for materials comparison must be undertaken; multiple shots should be acquired to construct a statistical distribution of characteristic velocities, wherein the differences among the statistical distributions may be more noticeable than direct comparison of a single data point limited by spatial and temporal resolutions. The differences observed in shock velocity (as discussed later) between the nm- and μm-sized Al were attributed to an increase in the microsecond-scale energy release, which drives the shockwave at times between 1–10 μs.

## 2.3 Shockwave Velocity Fitting

Empirical methods for data fitting for laser-induced shockwaves under these conditions has been explored in a previous report.[15] These fittings include the Sedov–Taylor fitting, a double exponential fitting, a fifth-order polynomial fitting, and the Dewey blast-wave fitting,[17] where typically in LASEM the polynomial fitting is used with a characteristic velocity for a given sample defined as the y-intercept (i.e., $t = 0$ s time step) of the fitting. These fittings and their advantages and disadvantages in fitting m-LASEM data are summarized in Table 1. The following combined effects allowing improved fitting using the nonpolynomial method are: 1) increased number of data points at <10 μs, including the data point at 1.25 μs, 2) smoother data traces as a result of the relative velocity measurement, and 3) improved fidelity of data drawn from <10 μs from the monochromatic imaging scheme. Other models that couple the initial expansion of the shockwave

at the ns timescale to its maximum velocity to further decay of the shockwave,[18] and which couple mass, momentum, and energy conservation,[19,20] have been explored but will be reported in more detail in a future tech report.

**Table 1 Summary of data models discussed in Gottfried and Barnes,[15] their functional forms, and their advantages and disadvantages. Capital letters denote fittting coefficients. Other values defined as follows: $\tau_1$ and $\tau_2$ are characteristic timescales equal to the inter-frame timing; $t_0$ is the time step of the first frame; $\alpha$ is the Sedov–Taylor critical exponent ($\alpha = 0.4$); $R_0$ is the initial shockwave radius/position; $\beta$ is a slowing coefficient due to drag from air; $v_{air}$ is the speed of sound in air.**

| Data fitting | Functional form | Advantages and disadvantages |
|---|---|---|
| Fifth-order polynomial | $v(t) = A\,t^5 + B\,t^4 - C\,t^3 + D\,t^2 - E\,t + F$ | Well fit for lower frame-rate data; correlates well to other bulk properties of HE materials; fitting fails at early times <5 μs; oscillates around data throughout time trace |
| Double exponential | $v(t) = C + A\exp\left(-\frac{t-t_0}{\tau_1}\right) + B\exp\left(-\frac{t-t_0}{\tau_2}\right)$ | Extreme sensitivity to input $\tau$ values on fitting; oscillates around data due to changing power law behavior |
| Sedov–Taylor drag model | $v(t) = A\alpha t^{\alpha-1} + R_0\beta t^{\beta-1}$ | Well fit at early times but begins to deviate from the data at late times (~40–50 μs) |
| Dewey fit | $v(t) = v_{\text{air}}\left(B + \frac{C}{1+v_{\text{air}}t} + \frac{D}{2(1+v_{\text{air}}t)\sqrt{\ln(1+v_{\text{air}}t)}}\right)$ | Crosses over from underestimating to overestimating data at roughly 5 μs; consistently highest $R^2$ value |

A typical data trace and these fittings are shown in log-log axes in Fig. 6. The log axes accentuate the differences in the fitting from the data at early times and show a general collapse in the fittings to the data at times past 30 μs. The fittings all have an $R^2 > 0.99$ (except for the polynomial fitting, which typically has an $R^2 \sim 0.97$) and deviate significantly from the data at times <6 μs under the high time-resolution imaging conditions. While the influence of these early time data points is sure to influence the polynomial fitting, the other three fits align much more closely with the data at these times. Of the remaining three choices, the Sedov–Taylor represents the data the best at early times but is the worst fit from approximately 10–30 μs. Likewise, the double exponential tends to oscillate between over- and underestimating the data across times up to approximately 30 μs. The Dewey fit slightly underestimates the early time data but tends to better represent the data

from 5–30 s. Thus, we use the Dewey fitting for velocity measurements when using this upgraded m-LASEM system.

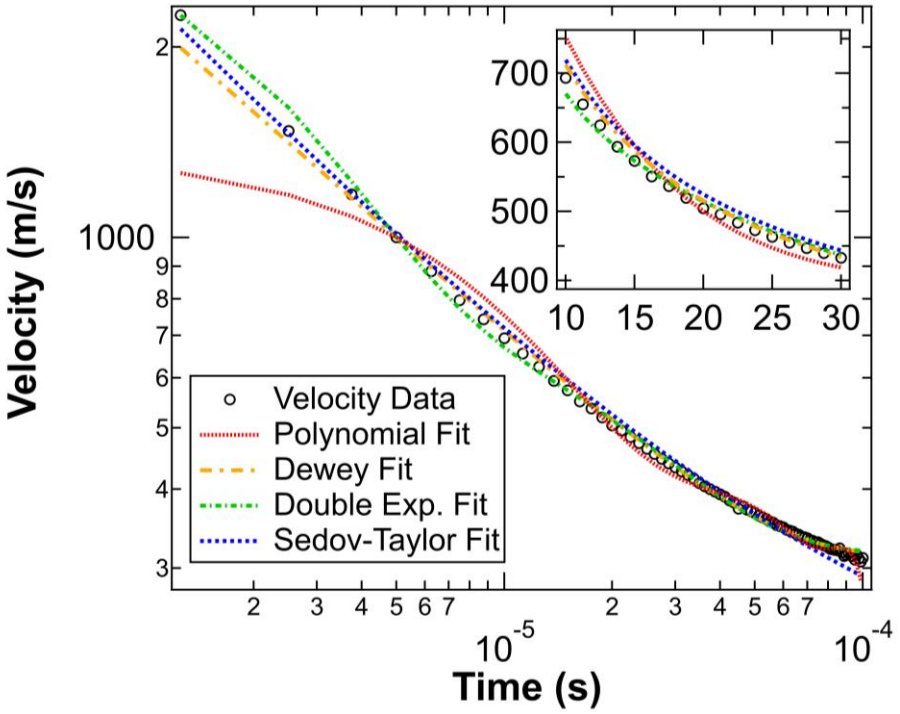


**Fig. 6 Representative velocity measurements drawn from the schlieren images of µm-size Al powder samples and the resultant data fitting via four different methods. The inset highlights the data region from 10–30 µs.**

## 2.4 Laser Energy and Shock Velocity Relationships

Under LASEM conditions, the laser energy used to ablate and excite material is significantly above its breakdown threshold. In addition, there is a subtle but present increase in shock velocity as a function of increasing laser energy across several hundreds of mJ.[21] The shot-to-shot variation of the shock velocity is expected to decrease as a function of increasing laser energy. To determine the shock velocity to laser energy relationship for m-LASEM, the voltage of the laser flashlamp was systematically increased and decreased. While the standard operating voltage of the laser used in m-LASEM is 1644 V, the change in laser energy across approximately 150 mJ is shown as a function for voltage in Fig. 7. The laser energy is measured by a beam power meter (Newport 919E-10-35-250 into 845-R power meter) directly below the focusing optic. The error bars in this trace are a result of small variations in both the laser output from shot to shot but also any slight variations in laser power meter positioning in the beam path and are typically <3 mJ. This range defines typical operating voltages used in the system;

confirming nominal power with a laser power meter before each instance of operating the system is necessary.

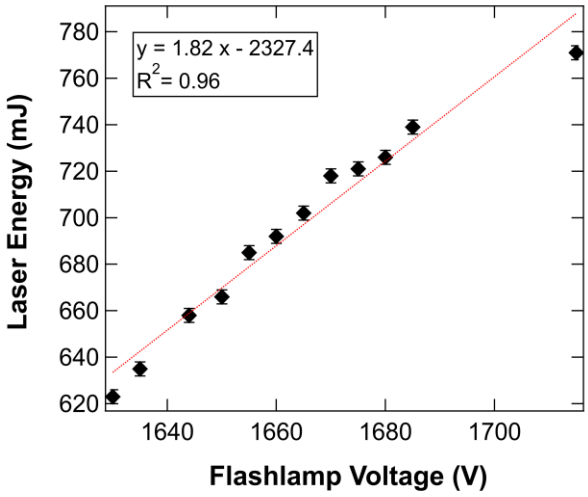


**Fig. 7 Laser energy as a function of flashlamp voltage, demonstrating a nearly linear relationship over the operating range used by m-LASEM**

The choice of a characteristic velocity to compare among samples as the primary relation to microsecond energy release is an arbitrary but important choice. For the original LASEM system, this characteristic velocity was chosen as the y-intercept of the polynomial fitting, which correlated well with bulk properties of HEs such as the detonation pressure and velocity.[21] Several of the nonpolynomial fittings listed in Table 1 have an asymptote at $t = 0$ s, and thus another time intercept must be used for comparison between samples if these fittings are implemented. Using the Dewey fitting, three intercepts of 13, 5, and 1 μs were selected; there is a natural tradeoff that occurs between the absolute value of the velocity difference between samples and the shot-to-shot deviation as one measures the characteristic velocity at later time intervals. That is, the earlier in time one measures the characteristic velocity, the more shot-to-shot variation is expected for a given sample, but a larger the difference between samples is expected. The characteristic velocity as measured at these three time steps for two samples of the blank tape and nm-Al at a variety of laser energies are shown in Fig. 8. It is clear from Fig. 8 that the difference in shock velocity is only weakly affected across the typical laser-energy operating range—increasing by only approximately 15 m/s over an approximately 120 mJ for the nm-Al measured at 13 μs. While this is a small difference, it does indicate continuous monitoring of the beam energy before and during a series of sample shots is recommended. Damage to the laser optics (e.g., from particles ejected from the sample surface coating the underside of the focusing lens) could potentially significantly decrease the laser pulse energy and disrupt the system calibration.

Further, the confidence interval on the shock velocity measurements, particularly for the nm-Al sample, decreases significantly at 13 µs. Given that the first velocity versus time data point among Al samples is quite similar, minimization of the confidence intervals achieved by defining the characteristic laser velocity at a later time intercept such as 13 µs is preferred. Defining the characteristic velocity at this time step allows for reactions that assist in driving the laser-induced shockwave from approximately 1–10 µs (i.e., the approximate time it takes the shockwave to transit the plasma region) to continue influencing the fitting and therefore velocity measurement.

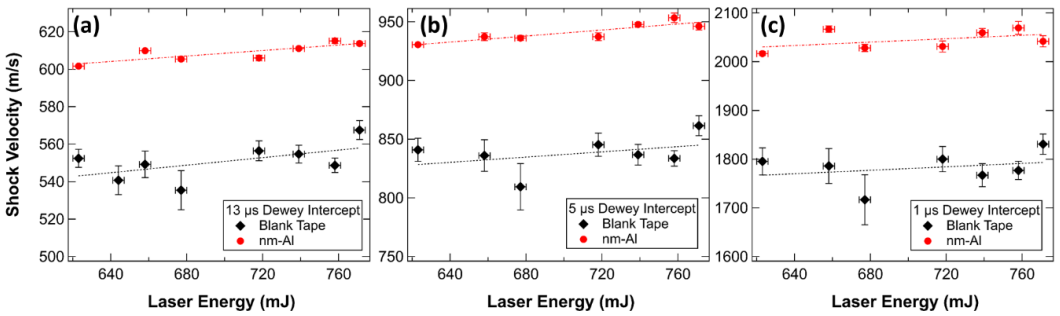


**Fig. 8 Shock velocity as measured for blank tape and nm-Al samples across a range of laser energies using a a) 13-µs Dewey blast fitting intercept, b) 5-µs intercept, and c) 1-µs intercept**

## 2.5 Shock Velocities Across a Survey of Metal Powders

To test the efficacy of the m-LASEM system in differentiating metal-based materials, a survey of powdered materials was collected. These materials include what would be considered "conventional" inputs for metal-based reactive materials such as boron (B) and Al. The characteristic velocity using a 13-µs intercept of the Dewey fitting is shown in Fig. 9. Among the same data, the Dewey intercept at 13 µs correlates well to the polynomial intercept at 13 µs, as shown in Fig. 10, suggesting the efficacy and relatability of the measurement techniques. Error bars on both the previous figures are 95% confidence intervals of the 20 shots collected for each sample. These materials came from a variety of sources, including commercial sources and from colleagues and collaborators. All the powders were in the µm size range, except for the nm-sized samples explicitly listed. Some trends observed in Fig. 9 are expected, such as metals with a high heat of oxidation (e.g., the conventional reactive materials like B and Al) having a higher shock velocity than inert materials like aluminum oxide ($Al_2O_3$). Further, reductions in particle size, such as moving from µm-sized to nm-sized Al particles, also results in an increase. Reactive, higher-density materials such as tungsten (W), zirconium (Zr), and molybdenum (Mo) show an increase over bulk and inert samples but fall below that of nm-sized materials with higher heats of oxidation. Lithium (Li) exhibits high

variability, possibly due to significant gas production or drilling into the bulk sample surface. These characteristic shock velocities do not directly correlate with thermophysical and materials properties including melting point, boiling point, density, thermal conductivity, specific heat, heat of oxidation (on atomic, per gram, and per volume bases), activation energy and rate constants of gas-phase metal oxidation rations (e.g., $M(g) + O_2(g) \rightarrow MO(g) + O(g)$ with $M$ as the metal species), latent heat of vaporization, ionization energy, or other surveyed properties.[22–25] This lack of first-order connections implies coupled, complex processes contributing to the shock velocity for these metal-based materials.

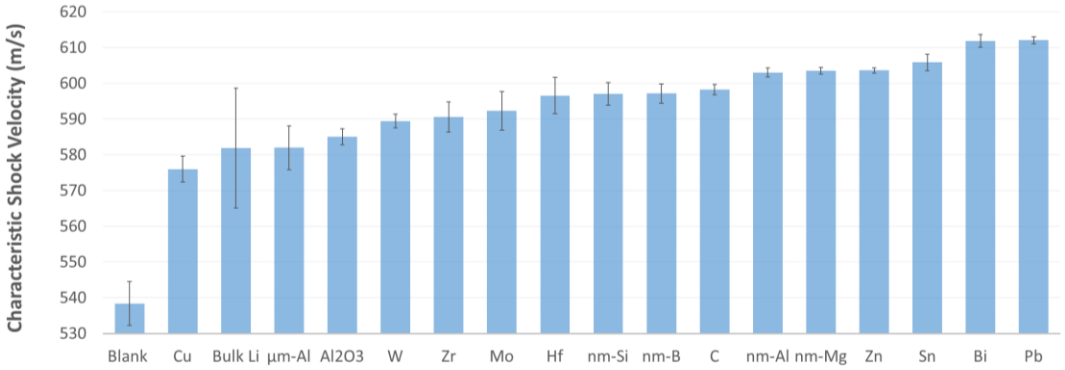


**Fig. 9 Characteristic laser-induced air-shock velocity measurements for metal powder samples, using the Dewey fitting with a 13-µs time intercept**

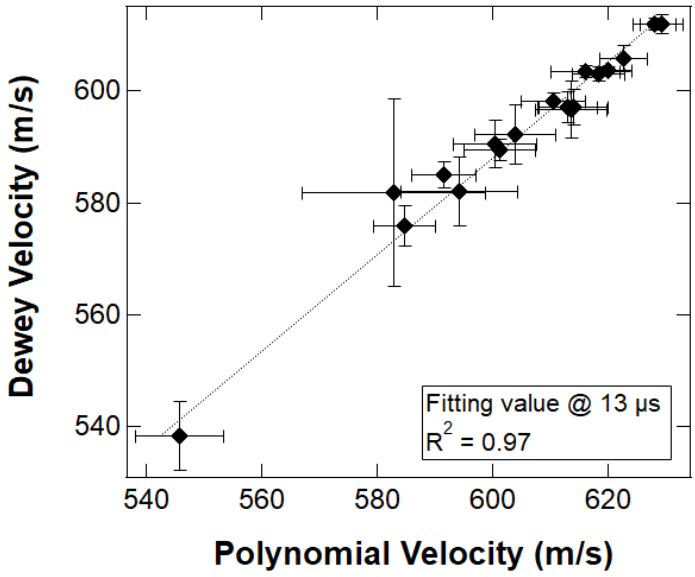


**Fig. 10 Relation between the Dewey and polynomial velocity fitting intercepts at 13 µs for the metal powder samples in Fig. 9**

There are some surprising results contained within this suite, including the high shock velocity of materials such as zinc (Zn), tin (Sn), bismuth (Bi), and lead (Pb).

These four specific materials have been shown to exhibit a low heat-absorption parameter,[26] which relates the ability for a material to dissipate heat to the amount of energy absorbed, through the factor

$$B \equiv \frac{KL_V}{dIC_p},$$

where $K$ is the thermal conductivity, $L_V$ is the latent heat of vaporization, $d$ is the skin depth of the material (defined in Pakhomov et al.[27]), $I$ is the laser irradiance, and $C_p$ is the specific heat, all in SI units. The smaller this $B$ factor, the more likely a material is to exhibit phase explosion (PE). PEs are a complex thermophysical phenomena wherein heating of a material causes rapid boiling of material below the surface, causing a thermal explosion and expulsion of particulate materials. Even though this value is remarkably small for Zn, Sn, Bi, and Pb, compared to the other materials (e.g., ~5–10× lower than Al) and these elements have the fastest laser-induced velocity, it is unclear whether the two properties are related. While it has been suggested that the PE process can develop and occur over much longer timescales than the original laser pulse, matching the time regime of relevance for acceleration and driving of the laser-induced plasma,[27] we see no correlation between $B$ calculated across all our materials at our laser wavelength (1064 nm) and irradiance (~ $1.1 \times 10^{10}$ W/cm$^2$), as shown in Fig. 11. Note the log x-axis in Fig. 11, meaning the $B$ spans several orders of magnitude under these conditions. Thus, it appears that under these conditions there are no strong first-order connections between the thermal properties (including those specifically related to PE) of a material and the shock velocities under m-LASEM conditions. We speculate that different metal-based materials could fall into different classes regarding dominant driving forces for the shockwave, such as high total heat of oxidation, low kinetic barriers to oxidation, or other possible mechanisms occurring simultaneously (e.g., PE). Further work of connecting fundamental material properties for metal-powder materials to their measured air-shock velocities under m-LASEM conditions is of great interest and is ongoing, including testing in oxygen-free and postdetonation gas environments to elucidate the effect of their relevant reactions with the metal species.

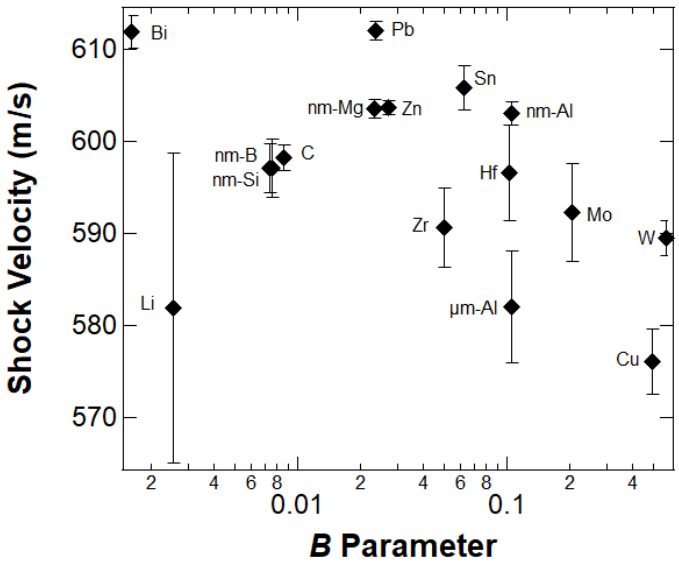


**Fig. 11 Shock velocity (measured using Dewey fitting at 13 μs) vs. *B* parameter relating to the propensity of a material to exhibit PE based off their innate thermal properties**

## 2.6 Shockwave Energy as a Function of Time

The Sedov–Taylor point explosion model is commonly used in describing the expansion of laser-induced shockwaves. A source energy term can be calculated from this model as the instantaneous driving force for this expansion. Previous efforts to calculate this instantaneous energy for LASEM have been explored with mixed results.[15,28] However, near-field models have been adapted to account for the source energy term contribution over time, as discussed by Roy et al.[29] Generally, data from m-LASEM shows no significant change in power-law behavior over a temporal regime of shockwave expansion from approximately 1–15 μs, as shown by the linearity in log-log axes of radius/position in Fig. 12a. Over this region, we can fit the radius data to a power law fitting $r = At^{\alpha}$ with $A$ and $\alpha$ as fitting parameters. Thus, under these conditions we can write the energy release in time as prescribed by Roy et al.[29] as

$$E(t) = K_2 A^5 \alpha^2 t^{5\alpha-2},$$

with $K_2$ of the form

$$K_2 = \frac{8\pi\rho_0(3\gamma-1)}{3(\gamma+1)^2(\gamma-1)},$$

containing gas-phase parameters $\rho_0$ as the density of air and $\gamma$ as the specific heat ratio of air. This form assumes the heat-capacity ratio of the source material (sample) is similar to that of air (~1.4). The classical value for $\alpha = 0.4$ can vary in

this model due to differences in the source term contribution. This expression provides the time-dependent energy release of a given sample, which represents a complex interplay of heat and mass transfer, plasma hydrodynamics, and most importantly, reactions occurring at the microsecond timescale that can be used as a relative metric between energetic samples. A representative energy versus time curve for μm-sized Al, nm-sized Al, and the blank tape is shown in Fig. 12b, and qualitatively matches those for other Al samples described in Roy et al.[29] Such measurements (at a time step of 13 μs) are decently correlated to the velocity measurements described previously, as shown in Figure 12c for a sampling of materials. Thus, the temporal energy, whether integrated or from a selected time step, may serve as an alternate metric of microsecond energy release to velocity while being conceptually and mechanistically relatable to physical processes such as chemical reactions. Such measurements are enabled by the upgraded imaging and data-processing techniques discussed in this work. Optimal methods of quantifying the energy release between disparate samples using the temporally resolved shock energy are in development as a future metric to compare among energetic samples.

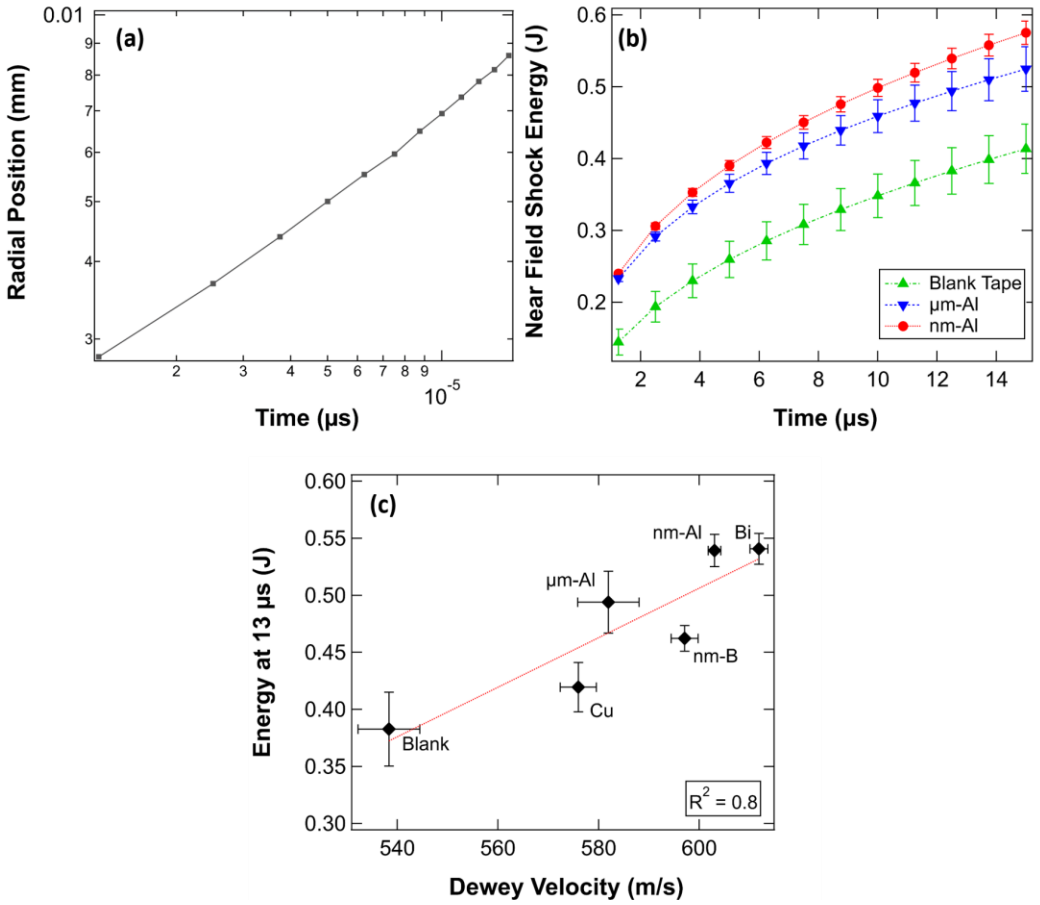


**Fig. 12 a) Log-log plot of laser-induced shockwave radius/position vs. time for a representative μm-size Al powder exhibiting a roughly linear curve, b) the calculated energy release as a function of time for the same sample (along with nm-Al and blank tape for comparison), c) the correlation between the measured shock energy at 13 μs and the shock velocity for a sampling of materials**

## 2.7 Correlations Between LASEM and m-LASEM

Given that the correlations with energetic performance have been established using the LASEM system, and due to the slight laser energy and imaging differences used with m-LASEM, we seek to draw correlations between samples tested on both systems. This correlation between systems helps establish confidence in the fidelity and repeatability of these measurements and allows for intermingling of data taken between the two systems. To this end, blank tape, inert samples (e.g., NIST $Al_2O_3$), μm-scale Al powders, nm-scale Al powders, and several novel reactive materials were tested with both LASEM and m-LASEM. The correlation of 13-μs intercept data under both the Dewey and polynomial fittings from m-LASEM to the LASEM polynomial fitting $t = 0$ s intercept are shown in Fig. 13. The data for m-LASEM for these two fits correlate well with the data taken from LASEM, while being more sensitive to subtle differences in similar materials (i.e., Al powders of varying size)

and able to penetrate through the optically thick plasma for very emissive materials at times <10 μs. Such a system is well suited to compare novel metal-based reactive materials in small quantities and assess their microsecond energy release performance prior to scale up. For ease of reference, a full comparison of the parameters used on the two systems is listed in Table 2.

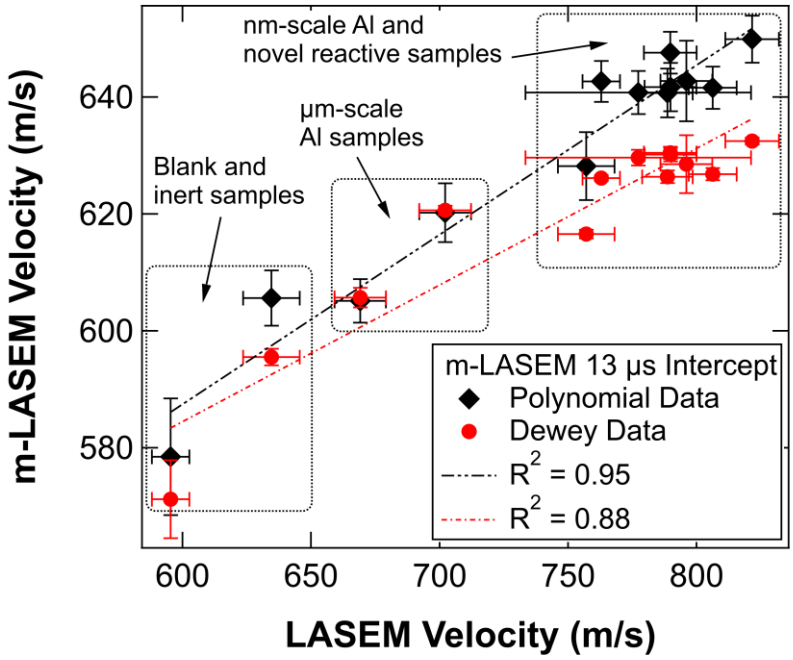


**Fig. 13 Linear correlations between Dewey and polynomial data taken at 13 μs with m-LASEM to the $t = 0$ s polynomial intercept data collected on the original LASEM system for a variety of materials**

**Table 2 Summary of LASEM vs. m-LASEM settings and characteristics and the relevant material categories**

| Property | LASEM | m-LASEM |
|---|---|---|
| Typical laser operating energy | ~610 mJ | ~660 mJ |
| Imaging specifications | Color, reported from either 80k or 420k fps, backlit by Hg-Xe arc lamp w/ broadband light | Monochromatic imaging, 800k fps, backlit by 640-nm imaging laser, bandpass filter on camera lens |
| Measurement technique | Fifth-order polynomial, characteristic velocity of $t = 0$ s (y-intercept), backwards difference velocity measurements | Dewey blast fitting, characteristic velocity at $t = 13$ µs, velocity measured relative to starting position/time |
| Data processing | 80k fps: all shock positions measured manually; 420k fps: First 5–10 frames manually measured due to plasma emission, remainder processed by moving window edge-detection algorithm;[15] data fitting completed separately | Automated edge detection using MATLAB image-processing toolbox, automated fitting |
| Utilization | HE materials, reactive materials with low visible emission at <20 µs | Metal-based reactive materials, samples with subtle differences in performance; Al samples |

## 3. Conclusion

In this work, we presented an upgraded imaging and data processing LASEM system for investigating reactive materials, which we colloquially call monochromatic LASEM, or m-LASEM. Through the combination of higher frame-rate imaging (i.e., 800,000 fps), using a single-wavelength imaging laser as the schlieren light source and a custom MATLAB data-processing script, we are able to collect and process data at over 10× the rate of previously reported LASEM. We have presented detailed accounts of the systems' timing and triggering that emphasize the importance of meticulous monitoring of laser pulse energy and camera trigger timing to obtain reasonable confidence intervals, which are required to distinguish energetic materials. Representative laser-induced shockwave data from this system has been presented and fitting techniques have been developed. Given the additional data points at early times in the shockwave expansion, we are able to utilize the Dewey equation as the primary fitting method, which we use to define the characteristic laser-induced shock velocity for a given energetic or reactive sample. We present several choices for this characteristic time (13, 5, and 1 µs) across a variety of laser energies between approximately 630–760 mJ. We find that the characteristic time of 13 µs provides adequate differentiation between

samples while minimizing the shot-to-shot variation in the sample. Further, it accounts for the continued release of energy due to reactive material sample reactions as the shockwave travels through the laser-induced plasma to times greater than 10 μs. This characteristic shock velocity for a given sample shows only weak dependence on the laser energies at such high power, increasing by roughly 3% over 15–20 mJ for the 13-μs fitting intercept, though it does imply continuous monitoring of the laser power is desirable for maximum repeatability. We analyzed a suite of metal-powder samples and find that under these measurement conditions we can differentiate between reactive and nonreactive samples; the results imply complex processes leading to the characteristic shock velocity for metal-based materials, which may not be solely determined by oxidation of the material. Finally, LASEM results from samples including the blank tape, inert materials, μm- and nm-sized Al powders, and several novel reactive materials are compared to m-LASEM data from the same samples and show good correlation. Thus, these approaches provide high-fidelity measurements of metal-based reactive materials and their microsecond energy release and are well suited to be used as a high-throughput laboratory-scale prescreening tool for such materials to assess their performance.

## 4. References


1. Gottfried JL. Influence of exothermic chemical reactions on laser-induced shock waves. Phys Chem Chem Phys. 2014;16:21452–21466.

2. Gottfried JL. Laboratory-scale method for estimating explosive performance from laser-induced shock waves. Propellants Explos Pyrotech. 2015;40:674–681.

3. Gottfried JL, Klapötke TM, Witkowski TG. Estimated detonation velocities for TKX-50, MAD-X1, BDNAPM, BTNPM, TKX-55 and DAAF using the laser-induced air shock from energetic materials technique. Propellants Explos Pyrotech. 2017;42:353–359.

4. Gottfried JL, Pesce-Rodriguez RA, Wu C-C. Validation of LASEM energy release predictions via detonation testing and analytical characterization. Army Research Laboratory (US); 2018 Oct. Report No.: ARL-TR-8557.

5. Gottfried JL, Pesce-Rodriguez RA, Farrow D, Dellinger J. Laboratory-scale investigation of the influence of ageing on the performance and sensitivity of an explosive containing ε-CL-20. Propellants Explos Pyrotech. 2018;43:616–625.

6. Gottfried JL, Dean SW, Wu C-C, DeLucia FC. Measuring fast and slow energy release from aluminum powders. AIP Conference Proceedings. 2020;2272:060016.

7. Gottfried JL, Bukowski EJ. Laser-shocked energetic materials with metal additives: evaluation of chemistry and detonation performance. Appl Opt. 2017;56:B47–B57.

8. Miller KK, Gottfried JL, Walck SD, Pantoya ML, Wu C-C. Plasma surface treatment of aluminum nanoparticles for energetic material applications. Combust Flame. 2019;206:211–213.

9. Wainwright ER, Dean SW, Lakshman SV, Weihs TP, Gottfried JL. Evaluating compositional effects on the laser-induced combustion and shock velocities of Al/Zr-based composite fuels. Combust Flame. 2019;213:357–368.

10. Gottfried JL, Dean SW, Collins ES, Wu C-C. Estimating the relative energy content of reactive materials using nanosecond-pulsed laser ablation. MRS Adv. 2018;3:875–886.

11. Gottfried JL. Higher time-resolution LASEM, part I: influence of aluminum morphology on laser-induced shock waves and chemistry. DEVCOM Army Research Laboratory (US); 2020 Aug. Report No.: ARL-TR-9020.

12. Gottfried JL, Dean SW, Wu C-C, DeLucia FC. Optimizing the performance of aluminized explosives: laser-based measurements of energy release and spectroscopic diagnostics. DEVCOM Army Research Laboratory (US); 2020 Apr. Report No.: ARL-TR-8934.

13. Settles GS, Hargather MJ. A review of recent developments in schlieren and shadowgraph techniques. Meas Sci Technol. 2017;28:042001.

14. Canny J. A computational approach to edge detection. IEEE Trans Pattern Anal Mach Intell. 1986;679–698.

15. Gottfried JL, Barnes BC. Higher time-resolution LASEM, part II: influence of plasma chemistry on the laser-induced shock waves of explosives. DEVCOM Army Research Laboratory (US); 2020 Aug. Report No.: ARL-TR-9026.

16. Wainwright ER, Dean SW, DeLucia Jr FC, Weihs TP, Gottfried JL. Effect of sample morphology on the spectral and spatiotemporal characteristics of laser-induced plasmas from aluminum. Appl Phys A. 2020;126:83.

17. Dewey JM. The air velocity in blast waves from TNT explosions. Proceedings of the Royal Society of London. Series A. Mathematical and Physical Sciences. 1964;279:366–385.

18. Wen S-B, Mao X, Liu C, Greif R, Russo R. Expansion and radiative cooling of the laser induced plasma. J Phys Conf Ser. 2007;59:072.

19. Chen X, Bian BM, Shen ZH, Lu J, Ni XW. Equations of laser-induced plasma shock wave motion in air. Microw Opt Technol Lett. 2003;38:75–79.

20. Schmitz TA, Koch J, Günther D, Zenobi R. Early plume and shock wave dynamics in atmospheric-pressure ultraviolet-laser ablation of different matrix-assisted laser ablation matrices. J Appl Phys. 2011;109:123106.

21. Gottfried JL. New laboratory-scale method for the determination of explosive performance from laser-induced shock waves. Army Research Laboratory (US); 2014 Mar. Report No.: ARL-TR-6844.

22. Chase JMW, Davies CA, Downey JR, Frurip DJ, McDonald RA, Syverud AN. NIST JANAF thermochemical tables, NIST standard reference database 13 1.0; 1985.

23. Fischer SH, Grubelich MC. Theoretical energy release of thermites, intermetallics, and combustible metals. Sandia National Laboratory; 1998 June. Report No.: SAND-98-1176C.

24. Linstrom PJ, Mallard WG. The NIST chemistry webbook: a chemical data resource on the internet. J Chem Eng Data. 2001;46:1059–1063.

25. Mallard WG, Westley F, Herron J, Hampson RF, Frizzell D. NIST chemical kinetics database. National Institute of Standards and Technology; 1992.

26. Dabby F, Paek U-C. High-intensity laser-induced vaporization and explosion of solid material. IEEE J Quantum Electron. 1972;8:106–111.

27. Pakhomov A, Thompson M, Gregory D. Laser-induced phase explosions in lead, tin and other elements: microsecond regime and UV-emission. J Phys D Appl Phys. 2003;36:2067.

28. Gottfried JL. Influence of exothermic chemical reactions on laser-induced shock waves. Phys Chem Chem Phys. 2014;16:21452–21466.

29. Roy S, Jiang N, Stauffer HU, Schmidt JB, Kulatilaka WD, Meyer TR, Bunker CE, Gord JR. Spatially and temporally resolved temperature and shock-speed measurements behind a laser-induced blast wave of energetic nanoparticles. J Appl Phys. 2013;113:184310.

## List of Symbols, Abbreviations, and Acronyms

| | |
|---|---|
| Al | aluminum |
| $Al_2O_3$ | aluminum oxide |
| B | boron |
| Bi | bismuth |
| DDG | digital delay generator |
| fps | frames per second |
| HE | high explosive |
| LASEM | laser-induced air shock from energetic materials |
| Li | lithium |
| m-LASEM | monochromatic laser-induced air shock from energetic materials |
| Mo | molybdenum |
| NIST | National Institute of Standards and Technology |
| Pb | lead |
| PE | phase explosion |
| PMT | photomultiplier tubes |
| Sn | tin |
| W | tungsten |
| Zn | zinc |
| Zr | zirconium |

1 (PDF) DEFENSE TECHNICAL INFORMATION CTR DTIC OCA

1 (PDF) DEVCOM ARL FCDD RLD DCI TECH LIB

2 (PDF) DEVCOM ARL FCDD RLW WA E WAINWRIGHT J GOTTFRIED